Brain refractive index measured *in vivo* with high-NA defocus-corrected full-field OCT and consequences for two-photon microscopy

Jonas Binding,[1, 2, 3, 4, *] Juliette Ben Arous,[1] Jean-François Léger,[1] Sylvain Gigan,[2] Claude Boccara[2] and Laurent Bourdieu[1]

[1] *IBENS, UMR 8197 CNRS and INSERM, Ecole Normale Supérieure, 46, Rue d'Ulm, 75005 Paris, France*
[2] *Institut Langevin "Ondes et Images", UMR7587 CNRS ESPCI ParisTech, 10, rue Vauquelin, 75005 Paris, France*
[3] *Max Planck Institute for Medical Research, Jahnstr. 29, 69120 Heidelberg, Germany*
[4] *Fondation Pierre-Gilles de Gennes pour la Recherche, 29 rue d'Ulm, 75005 Paris, France*
**jonas.binding@espci.fr*

Abstract: Two-photon laser scanning microscopy (2PLSM) is an important tool for *in vivo* tissue imaging with sub-cellular resolution, but the penetration depth of current systems is potentially limited by sample-induced optical aberrations. To quantify these, we measured the refractive index n' in the somatosensory cortex of 7 rats *in vivo* using defocus optimization in full-field optical coherence tomography (ff-OCT). We found n' to be independent of imaging depth or rat age. From these measurements, we calculated that two-photon imaging beyond 200µm into the cortex is limited by spherical aberration, indicating that adaptive optics will improve imaging depth.

OCIS codes: (080.1010) Aberrations (global); (170.6935) Tissue characterization; (170.4500) Optical coherence tomography; (180.4315) Nonlinear microscopy; (290.0290) Scattering; (290.3030) Index measurements; (110.4500) Optical coherence tomography; (110.0113) Imaging through turbid media; (110.1080) Active or adaptive optics.

References and Links

1. P. Theer, M. T. Hasan, and W. Denk, "Two-photon imaging to a depth of 1000 microm in living brains by use of a Ti:Al2O3 regenerative amplifier," Opt. Lett. **28**(12), 1022–1024 (2003).
2. K. Svoboda, W. Denk, D. Kleinfeld, and D. W. Tank, "In vivo dendritic calcium dynamics in neocortical pyramidal neurons," Nature **385**(6612), 161–165 (1997).
3. D. Débarre, E. J. Botcherby, T. Watanabe, S. Srinivas, M. J. Booth, and T. Wilson, "Image-based adaptive optics for two-photon microscopy," Opt. Lett. **34**(16), 2495–2497 (2009).
4. N. Ji, D. E. Milkie, and E. Betzig, "Adaptive optics via pupil segmentation for high-resolution imaging in biological tissues," Nat. Methods **7**(2), 141–147 (2009).
5. J. M. Girkin, J. Vijverberg, M. Orazio, S. Poland, and A. J. Wright, "Adaptive optics in confocal and two-photon microscopy of rat brain: a single correction per optical section," in *Multiphoton Microscopy in the Biomedical Sciences VII*(SPIE, San Jose, CA, USA, 2007), pp. 64420T–64427.
6. M. Rueckel, J. A. Mack-Bucher, and W. Denk, "Adaptive wavefront correction in two-photon microscopy using coherence-gated wavefront sensing," Proc. Natl. Acad. Sci. U.S.A. **103**(46), 17137–17142 (2006).
7. W. Gottschalk, "Ein Messverfahren zur Bestimmung der optischen Parameter biologischer Gewebe in vitro," (Universität Karlsruhe, Karlsruhe, 1993), p. 172.
8. N. Lue, J. Bewersdorf, M. D. Lessard, K. Badizadegan, R. R. Dasari, M. S. Feld, and G. Popescu, "Tissue refractometry using Hilbert phase microscopy," Opt. Lett. **32**(24), 3522–3524 (2007).
9. B. Rappaz, P. Marquet, E. Cuche, Y. Emery, C. Depeursinge, and P. Magistretti, "Measurement of the integral refractive index and dynamic cell morphometry of living cells with digital holographic microscopy," Opt. Express **13**(23), 9361–9373 (2005).
10. S. N. Roper, M. D. Moores, G. V. Gelikonov, F. I. Feldchtein, N. M. Beach, M. A. King, V. M. Gelikonov, A. M. Sergeev, and D. H. Reitze, "In vivo detection of experimentally induced cortical dysgenesis in the adult rat neocortex using optical coherence tomography," J. Neurosci. Methods **80**(1), 91–98 (1998).
11. G. J. Tearney, M. E. Brezinski, J. F. Southern, B. E. Bouma, M. R. Hee, and J. G. Fujimoto, "Determination of the refractive index of highly scattering human tissue by optical coherence tomography," Opt. Lett. **20**(21), 2258–2260 (1995).

#139111 - $15.00 USD Received 7 Dec 2010; revised 24 Jan 2011; accepted 2 Feb 2011; published 28 Feb 2011

12. S. Labiau, G. David, S. Gigan, and A. C. Boccara, "Defocus test and defocus correction in full-field optical coherence tomography," Opt. Lett. **34**(10), 1576–1578 (2009).
13. A. Dubois, L. Vabre, A. C. Boccara, and E. Beaurepaire, "High-resolution full-field optical coherence tomography with a Linnik microscope," Appl. Opt. **41**(4), 805–812 (2002).
14. L. Vabre, A. Dubois, and A. C. Boccara, "Thermal-light full-field optical coherence tomography," Opt. Lett. **27**(7), 530–532 (2002).
15. A. F. Fercher, "Optical Coherence Tomography," J. Biomed. Opt. **1**(2), 157–173 (1996).
16. J. G. Fujimoto, M. E. Brezinski, G. J. Tearney, S. A. Boppart, B. Bouma, M. R. Hee, J. F. Southern, and E. A. Swanson, "Optical biopsy and imaging using optical coherence tomography," Nat. Med. **1**(9), 970–972 (1995).
17. G. J. Tearney, B. E. Bouma, S. A. Boppart, B. Golubovic, E. A. Swanson, and J. G. Fujimoto, "Rapid acquisition of in vivo biological images by use of optical coherence tomography," Opt. Lett. **21**(17), 1408–1410 (1996).
18. S. A. Alexandrov, A. V. Zvyagin, K. K. Silva, and D. D. Sampson, "Bifocal optical coherenc refractometry of turbid media," Opt. Lett. **28**(2), 117–119 (2003).
19. A. Knuettel, and M. Boehlau-Godau, "Spatially confined and temporally resolved refractive index and scattering evaluation in human skin performed with optical coherence tomography," J. Biomed. Opt. **5**(1), 83–92 (2000).
20. A. Zvyagin, K. K. M. B. Silva, S. Alexandrov, T. Hillman, J. Armstrong, T. Tsuzuki, and D. Sampson, "Refractive index tomography of turbid media by bifocal optical coherence refractometry," Opt. Express **11**(25), 3503–3517 (2003).
21. P. Török, P. Varga, Z. Laczik, and G. R. Booker, "Electromagnetic diffraction of light focused through a planar interface between materials of mismatched refractive indices: an integral representation," J. Opt. Soc. Am. A **12**(2), 325–332 (1995).
22. D. Debarre, M. J. Booth, and T. Wilson, "Image based adaptive optics through optimisation of low spatial frequencies," Opt. Express **15**(13), 8176–8190 (2007).
23. M. Daimon, and A. Masumura, "Measurement of the refractive index of distilled water from the near-infrared region to the ultraviolet region," Appl. Opt. **46**(18), 3811–3820 (2007).
24. A. Egner, and S. W. Hell, "Equivalence of the Huygens-Fresnel and Debye approach for the calculation of high aperture point-spread functions in the presence of refractive index mismatch," J. Microsc. **193**(3), 244–249 (1999).
25. E. J. Botcherby, R. Juskaitis, M. J. Booth, and T. Wilson, "Aberration-free optical refocusing in high numerical aperture microscopy," Opt. Lett. **32**(14), 2007–2009 (2007).
26. J. Binding, "Adaptive Optics in Two-Photon-Microscopy," in *Fakultät für Physik und Astronomie*(Ruprecht-Karls-Universität Heidelberg, Heidelberg, 2008), p. 99.
27. M. Born, and E. Wolf, *Principles of Optics* (Cambridge University Press, Cambridge, U.K., 1999).
28. M. Oheim, E. Beaurepaire, E. Chaigneau, J. Mertz, and S. Charpak, "Two-photon microscopy in brain tissue: parameters influencing the imaging depth," J. Neurosci. Methods **111**(1), 29–37 (2001).
29. D. Sacchet, J. Moreau, P. Georges, and A. Dubois, "Simultaneous dual-band ultra-high resolution full-field optical coherence tomography," Opt. Express **16**(24), 19434–19446 (2008).
30. D. Kobat, M. E. Durst, N. Nishimura, A. W. Wong, C. B. Schaffer, and C. Xu, "Deep tissue multiphoton microscopy using longer wavelength excitation," Opt. Express **17**(16), 13354–13364 (2009).
31. H. Ding, J. Q. Lu, W. A. Wooden, P. J. Kragel, and X. H. Hu, "Refractive indices of human skin tissues at eight wavelengths and estimated dispersion relations between 300 and 1600 nm," Phys. Med. Biol. **51**(6), 1479–1489 (2006).

Introduction

For many biological imaging applications, light imaging provides a good compromise between resolution, penetration depth and non-invasiveness. Still, optimizing the penetration depth of optical techniques is crucial for *in vivo* imaging in biological tissues such as the animal brain. Due to decreased scattering at longer excitation wavelengths, two-photon laser scanning microscopy (2PLSM) has improved depth penetration, which is ultimately limited by surface fluorescence generation [1]. 2PLSM has, therefore, become an established method used for functional *in vivo* imaging of rat cortex with sub-cellular resolution [2].

In addition to light scattering, optical aberrations enlarge the focus and decrease two-photon excitation efficiency. Thus, a decrease in possible penetration depth is expected when the refractive index of the sample does not exactly match the immersion medium. Even if the refractive index is homogeneous, the layer between the immersion medium and selected sample slice will cause spherical aberration. It is possible that part of the signal loss currently attributed to the scattering of excitation light is actually due to optical aberrations. Attempts to implement adaptive optics in 2PLSM [3] aim at correcting for these sample-induced aberrations.

For two reasons, there is still not enough quantitative data on how strong these aberrations are in biological tissues and, in particular, in the rat brain. First, biological samples usually do not contain sufficiently reliable point sources to perform an evaluation of resolution loss with

#139111 - $15.00 USD Received 7 Dec 2010; revised 24 Jan 2011; accepted 2 Feb 2011; published 28 Feb 2011

depth. Second, an ideal sensor for measuring *in vivo* aberrations at high depths in scattering tissue like the rat cortex has, to our knowledge, not been demonstrated. Consequently it is uncertain how much signal and resolution can be gained by correcting these optical aberrations [3–6].

In the absence of a precise wavefront sensor, a lower bound for the scale of aberrations encountered can be deduced from the refractive index (and possibly from its spatial fluctuations) of the sample, given the numerical aperture (NA) and immersion medium of the microscope objective used. The refractive index of brain tissue has been measured *in vitro* [7–10], but no precise *in vivo* measurement was found in the literature. Both fixed tissue and acute slices are expected to have modified optical properties due to changes in the mechanical and chemical environments compared to *in vivo* tissue, and are therefore not optimal for measuring the refractive index.

In this work, we measured the refractive index of the rat somatosensory cortex *in vivo* using defocus optimization [11–12] in full-field optical coherence tomography (ff-OCT) [13–14]. Optical coherence tomography (OCT) is a powerful imaging technique used in highly scattering tissues, where backscattered light from a certain depth is selected interferometrically. This allows two- and three-dimensional imaging using the local backscattering coefficient as a source of endogenous contrast [15–17]. As one of the rare epi-configuration microscopy systems which is sensitive to defocus (axial focus shift), OCT is perfectly suited for refractive index measurements in the living cortex, where a transmission measurement is not possible. This measurement of the refractive index in the rat brain allowed us to estimate the signal intensity loss as a function of penetration depth in 2PLSM.

Materials and methods

Ff-OCT setup

A custom-made ff-OCT microscope was used to image the somatosensory cortex of anesthetized rats. The microscope (Fig. 1) consisted of a low coherence light source (250W halogen lamp), with the standard Köhler microscope illumination, a Linnik interferometer (i.e. a Michelson interferometer with an objective in each arm), a tube lens and an InGaAs camera. The water immersion objectives used were Zeiss IR-Achroplan 40x/0.8W. The effective spectrum of the light source including optical components (as well as water) and the detector was centered on $\lambda = 1100$ nm and had a full width at half maximum (FWHM) of around 200nm. For dispersion correction, a cover slip identical to that protecting the rat's cortex (see below) was placed in the reference arm of the interferometer. To avoid the reflection caused by the coverslip hitting the camera, the coverslip was tilted slightly. A 50cm doublet was used as a tube lens to image the sample and the reference arm mirror onto the InGaAs camera (Xeva-1.7-320, Xenics Infrared Solutions, Leuven, Belgium). The sensor chip had 320x256 pixels and was operated at its maximum frequency of 66Hz, triggered by a NI 6722 digital I/O board (National Instruments, Austin, Texas) and controlled by the software, LightCT (LLTech, Paris). Both the sample z-position and the relative arm length could be changed with two motorized linear stages (M-VP-25XA, Newport). A synchronized rectangular 33 Hz signal drove the Piezo Linear Stage Actuator (PI P-753.11C, Physik Instrumente [PI] GmbH, Karlsruhe) onto which the reference arm mirror was mounted. The piezo actuator amplitude was adapted to produce a change in reference arm length of $\lambda/2$, so that the relative phase between both arms of the interferometer would change by π. Taking the difference of subsequent camera images would therefore separate the interference signal (more exactly: the projection of the interfering electromagnetic field onto the real axis) from the background light, implementing a two-step phase stepping protocol. LightCT running on standard PC allowed real-time display of these OCT images at 33 Hz.

#139111 - $15.00 USD Received 7 Dec 2010; revised 24 Jan 2011; accepted 2 Feb 2011; published 28 Feb 2011

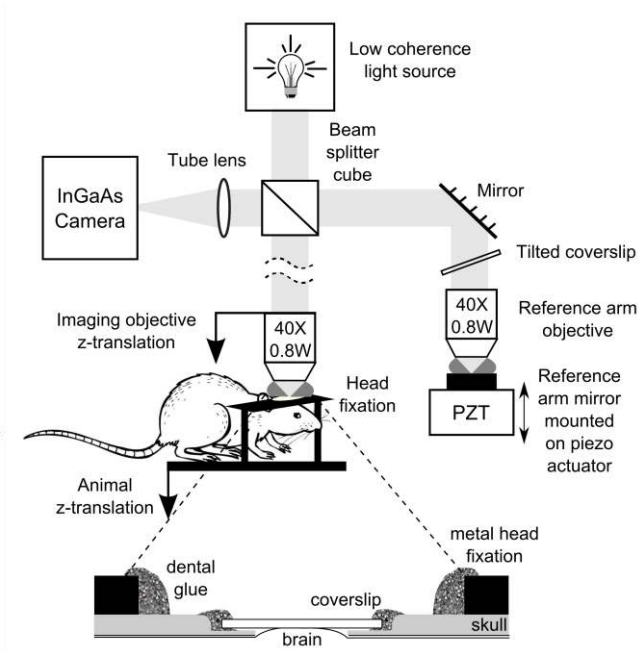

Fig. 1. Ff- OCT setup and sample preparation. Light from a low-coherence source enters a Linnik interferometer. The sample arm consists of a microscope objective on a motorized linear translation stage allowing axial movement and of the sample, which is equally translatable along the optical axis. The animal is held by a metal head fixation plate glued to its skull around the craniotomy, which consists of a cover slip glued onto the thinned bone around the actual opening, where the brain tissue comes into direct contact with the cover slip. The reference arm consists of a folding mirror, a cover slip to compensate for dispersion from the cover slip on the rat brain, an objective identical to the sample objective and a reference mirror mounted on a piezo actuator for phase-stepping. The focal planes of both objectives are imaged using a lens doublet serving as tube lens onto an InGaAs camera. The piezo, camera and both motorized stages are controlled by a standard PC running Light-CT software.

Animal preparation

All surgical procedures were in accordance with the European Community guidelines on the care and use of animals (86/609/CEE, CE official journal L358, 18th December 1986), French legislation (décret no. 97/748, 19th October 1987, J. O. République française, 20th October 1987), and the recommendations of the CNRS.

Three 3 week old (P20-21; weight ~80g), two 6 week old (P45-46; weight ~250g) and two 12 week old (P86-87; weight ~400g) male Wistar rats were included in this study. Rats were anesthetized by urethane injection (1.5 g/kg). Supplementary doses of urethane were applied when necessary. The body temperature of the animal was held at 38°C by a heating blanket during the surgery and the imaging. Animals were maintained in a stereotaxic frame during the surgical procedure. A craniotomy (~3mm in diameter) centered over the somatosensory cortex was performed on the rat's left hemisphere and the dura mater was removed. The craniotomy was sealed with a 5mm diameter coverslip, which was glued onto the thinned skull surrounding the hole. Thinning was performed to bring the coverslip in close contact with the brain of the animal, in order to prevent movement of the brain during the imaging procedure.

For ff-OCT imaging, the animal was stabilized with a metal holder glued to its skull (Fig. 1). At the end of the experiments, rats were injected with a lethal dose of urethane.

Principle of refractive index measurement based on defocus correction

For the measurement of the refractive index of the sample, the sensitivity of high NA optical coherence tomography to defocus aberration was exploited (Fig. 2). In the following,

#139111 - $15.00 USD Received 7 Dec 2010; revised 24 Jan 2011; accepted 2 Feb 2011; published 28 Feb 2011

unprimed variable names refer to properties of water and primed variables to those of tissue. When imaging with a correctly aligned system at the surface of a biological sample, the focal plane of the microscope objective coincides with the center of the coherence volume defining the sectioning volume of the OCT system (Fig. 2a). When imaging deeper into a sample with a phase refractive index n' larger than that of the immersion medium n, refraction at the surface causes the actual focus z_A of the objective to be enlarged and shifted deeper into the sample with respect to the nominal focus z_N (Fig. 2b). At the same time, the coherence volume penetrates the tissue slower than the nominal focus due to the increased group refractive index n'_g (defined as $n'_g = c/v'_g$ with c being the vacuum speed of light and v'_g the group velocity in matter) (Fig. 2b). This discrepancy between coherence volume and actual focus results in a reduction of interference contrast (i.e. in a loss in OCT signal). This signal loss is therefore related to the optical properties of the sample and for a proper analysis of this effect, we have to take n' and its dispersion into account and differentiate between n' and n'_g of the sample.

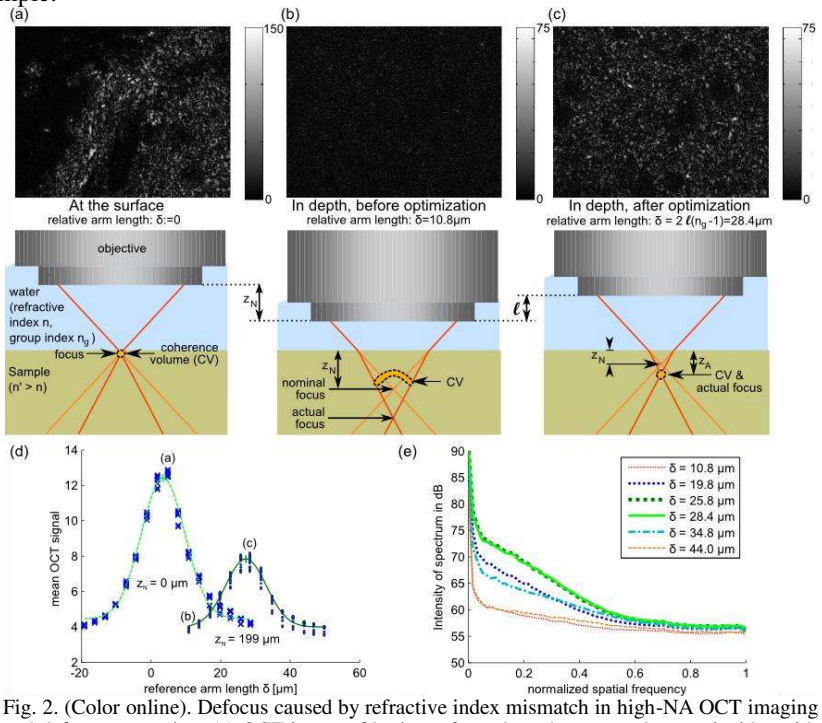

Fig. 2. (Color online). Defocus caused by refractive index mismatch in high-NA OCT imaging and defocus correction. (a) OCT image of brain surface; the coherence volume coincides with the focus of the objective, leading to good imaging limited only by diffraction and speckle. The relative arm length δ is by definition 0. (b) When imaging at a nominal depth z_N of 205µm below the tissue surface, the refractive index mismatch causes the coherence volume to move upwards and the actual focus z_A to move downwards with respect to z_N. The plane imaged with OCT, defined by the position of the coherence volume (CV), contains hardly any structure due to defocus aberration. This is equally true at relative arm length δ = 0 (not shown) and at the non-optimized relative arm length δ = 10.8µm shown here. (c) Moving the objective by a distance l and simultaneously changing the reference arm length by $\delta = 2\ l\ (n_g - 1)$ allows the actual focus z_A to be brought into coincidence with the coherence volume, restoring OCT signal and revealing the spatial reflectivity variations of the sample. Note that this decreases the nominal imaging depth by l to z_N= 199µm. (d) OCT signal depends on the correct setting of the reference arm length δ. The data points corresponding to the images shown in a-c are indicated by the corresponding letters. A Gaussian with a baseline is fitted to the data to find the position of the peak, which corresponds to the optimal reference arm length δ at that depth z_N. Due to defocus, the optimal reference arm length δ at z_N = 199µm has shifted to higher values compared to z_N = 0 µm. (e) The spatial frequency content of images for different reference arm lengths δ shows image degradation (loss in low and medium spatial frequency content) when a non-optimal reference arm length introduces defocus.

#139111 - $15.00 USD Received 7 Dec 2010; revised 24 Jan 2011; accepted 2 Feb 2011; published 28 Feb 2011

To compensate for this signal loss and to maximize the OCT signal, it has been proposed to change the reference arm length to move the coherence volume into the position of the actual focus [11], but this maximization scheme changes the depth of the imaged plane inside the sample. Such an optimization is, therefore, biased by the exponential signal decay with imaging depth, and by the sample structure. To avoid these sources of bias, it is preferable to keep the coherence volume at a constant depth inside the sample and move the actual focus into this same position [12] (Fig. 2c). If dry objectives were being used, this could be achieved by moving only the sample objective and keeping reference arm and sample fixed. Due to the water immersion (group index n_g), a movement l of the sample objective away from the sample increases the (paraxial) optical path in water by $2\ n_g\ l$, while the optical path in air only decreases by $2\ l$. To keep the coherence volume in the same position inside the tissue, displacement l of the sample objective should be associated by a displacement $d(l)$ of the reference arm, corresponding to an increase of the reference arm length $\delta(l) = 2d(l) = 2l(n_g\text{-}l)$.

In summary, a concerted movement of the sample objective l and the reference arm $d(l)$ leads to an optimization scheme where the imaged plane remains fixed inside the sample, while the actual focus of the objective scans through different depths. Experimentally, images were taken in successive associated positions (l, $d(l)$) and an image-based metric (see below) was used to experimentally determine which positions (l, $d(l)$) centered the actual focus on the coherence volume (Fig. 2d). In the following, optimal positions (l, $d(l)$) will simply be referred to as the optimal reference arm position d (or length δ).

From the nominal focus z_N and the optimal reference arm length δ, the refractive index n' of the sample can, in principle, be inferred. Previous calculations of the relationship between n' and δ at a given z_N have focused on paraxial or marginal ray analysis and were only used in conjunction with low NA (i.e. below 0.2). Even though some papers presented formulae differentiating between n' and n'_g, calculations were always performed assuming zero dispersion in all media involved (i.e. $n = n_g$, $n' = n'_g$) [11, 18–20].

While these approximations greatly simplify the calculations, they are certainly inadequate for the NA 0.8 objectives used I n this work. The use of high-NA objectives increases the defocus aberration and, therefore, the sensitivity to the refractive index, at the expense of a more complicated calculation. Even monochromatically, the point of best focus in presence of a refractive index mismatch is no longer described correctly by the paraxial theory in the case of high NA objectives. Since the immersion water, which has a significant level of dispersion in the near infrared wavelength region, served as a reference medium, we felt it necessary to revisit the issue of the influence of dispersion on the refractive index determination. The experimental precision of our data goes beyond the 1-2% limit presented in previous work [11–12, 18–20], which means dispersion can no longer be neglected.

In principle, the sample should be described as a volume with a certain mean refractive index n', a given amount of dispersion $n'(\lambda)$ and a random homogeneous distribution of scatterers. The light of all different wavelengths and incident angles is focused by the microscope objective into this volume, where each scatterer produces secondary spherical waves whose amplitudes and phases depend on the amplitude and phase of the incoming waves at the position of the scatterer. These secondary waves will re-enter the microscope objective and ultimately be transmitted to the detector, where each of them interferes with the corresponding wave from the reference arm. What the detector measures is the power from the sum over all these angles and wavelengths.

Without a refractive index mismatch, a scatterer at the geometric focus will produce secondary waves which are perfectly in phase with the waves in the reference arm, independent of angle and wavelength, maximizing constructive interference. Any effect which causes a dephasing for some of the waves will decrease interference and, thereby, OCT signal.

When treating a refractive index mismatch in the paraxial approximation, the main dephasing comes from the dispersion. Since all waves travel in essentially the same direction, the dispersion can (as long as it is linear) be described by a group velocity, i.e. the medium

#139111 - $15.00 USD Received 7 Dec 2010; revised 24 Jan 2011; accepted 2 Feb 2011; published 28 Feb 2011

group refractive index enters as a new independent variable [19]. In contrast, when dispersion in both media can be neglected, the main dephasing effect comes from the fact that marginal rays travel a much longer distance through the index-mismatched medium, causing their optical path length to be different from the more paraxial rays. In this case, the dephasing depends on the wave's incident and reflecting angle, which can be described by a generalized wavefront $\psi(\alpha_{in},\alpha_{out})$ (see below).

When both NA and dispersion become important, the concept of group velocity is not helpful anymore since wave components with different wavelengths will not only propagate with different speeds, but will also be refracted by different angles. The only rigorous solution is to examine directly the total intensity I on a given pixel of the detector after integrating the amplitude of the electromagnetic field E over all possible wavelengths and incident and reflection angles and summing over both interferometer arms:

$$I = \left|E_{SMP} + E_{REF}\right|^2 = \left|E_{SMP}\right|^2 + \left|E_{REF}\right|^2 + 2\Re(E^*_{SMP}E_{REF}) \quad (1)$$

where the first two terms correspond to the incoherent background intensity from the sample and reference arms, which are essentially constant, and the third term, which can be separated out from the background by phase stepping, has the form

$$E^*_{SMP}E_{REF} = \int d\lambda \int 2\pi\alpha_{in} d\alpha_{in} \int 2\pi\alpha_{out} d\alpha_{out} K(\lambda,\alpha_{in},\alpha_{out}) \quad (2)$$

and is a function of sample refractive index n'(λ) and reference arm length δ through $K(\lambda,\alpha_{in},\alpha_{out})$.

In principle, for an exact expression for Eq. (2), one would even need to sum over all scatterers in the sample and average over all possible realizations of random scatterer configurations. However, since we are only interested in the case where the OCT signal is maximal, these summation and averaging operations can be replaced by a properly placed single scatterer. Due to symmetry it must sit on the optical axis, while its axial position z_A is optimized numerically to maximize OCT signal.

The term $K(\lambda,\alpha_{in},\alpha_{out})$ describes the product $E^*_{SMP}.E_{REF}$ for a given wavelength, incidence angle α_{in} and reflection angle α_{out}. Since phase effects will largely dominate any amplitude effects in the triple integral, we will neglect the reflectivity of the reference arm mirror, the scattering cross section and anisotropy of the scatterers as well as any amplitude effects caused by propagation. This is particularly true since we are only interested in the position of the maximum with respect to n'(λ) and δ, not in the actual value of the integral. We are therefore left with

$$K(\lambda,\alpha_{in},\alpha_{out}) = E^*_{SMP}E_{REF} = e^{-i\frac{2\pi}{\lambda}[\delta_0+\Psi(\lambda,\alpha_{in},\alpha_{out})]} e^{+i\frac{2\pi}{\lambda}[\delta_0+\delta]} = e^{-i\frac{2\pi}{\lambda}[\Psi(\lambda,\alpha_{in},\alpha_{out})-\delta]} \quad (3)$$

where δ_0 is the total optical path for light reflected back from the focus in one arm of the interferometer when the focus is at the sample surface and δ is the additional length added to the reference arm to maximize the OCT signal. The generalized wavefront $\psi(\lambda,\alpha_{in},\alpha_{out})$ describes the additional optical path in the sample arm due to refractive index mismatch when the nominal imaging depth inside the sample is z_N and the scatterer is in depth z_A below the sample surface. It can be expressed as the sum of two identical terms for the incoming and scattered light paths

$$\Psi(\lambda,\alpha_{in},\alpha_{out}) = \Psi(\lambda,\alpha_{in}) + \Psi(\lambda,\alpha_{out}) \quad (4)$$

where α_{in} and α_{out} are the angles of the incoming and outgoing light rays in water, measured with respect to the optical axis. Both terms can be described by [21]

$$\Psi(\lambda,\alpha) = z_N n(\lambda)\cos(\alpha) - z_A n'(\lambda)\cos(\alpha') = z_N n(\lambda)\cos(\alpha) - z_A\sqrt{n'(\lambda)^2 - n(\lambda)^2\sin^2(\alpha)} \quad (5)$$

#139111 - $15.00 USD Received 7 Dec 2010; revised 24 Jan 2011; accepted 2 Feb 2011; published 28 Feb 2011

where unprimed angles are in water and primed angles in the tissue and the second equation follows from Snell's law of refraction. For the full generalized wavefront this gives

$$\begin{aligned}\Psi(\lambda,\alpha_{in},\alpha_{out}) &= \Psi(\lambda,\alpha_{in})+\Psi(\lambda,\alpha_{out})\\ &= z_N n(\lambda)\left(\cos(\alpha_{in})-\cos(\alpha_{out})\right)\\ &-z_A\left(\sqrt{n'(\lambda)^2-n(\lambda)^2\sin^2(\alpha_{in})}-\sqrt{n'(\lambda)^2-n(\lambda)^2\sin^2(\alpha_{out})}\right)\end{aligned} \tag{6}$$

This form of the wavefront assumes that the sample surface is flat and orthogonal to the optical axis.

For each nominal focus z_N, an optimal reference arm length $\delta = 2d$ is experimentally determined. For this pair of values (z_N, δ), we can, in principle, determine the corresponding refractive index n' from Eq. (2) by maximizing the integral with respect to n' and z_A. However, n' depends not directly on δ and z_N but only on their ratio δ/z_N (with an error of around 10^{-3} in the range needed here; see theory curves for n' = 1.33/1.34/… in Fig. 3). This simplifies the analysis in that a constant slope in a z_N vs. δ plot implies a depth-independent refractive index. The value of n' can, in this case, be determined from the slope $s = \delta/z_N$ of a linear least squares fit to the data from all available depths by optimizing Eq. (2) at an arbitrary nominal depth, e.g. $z_N = 500$ µm, $\delta = s\, z_N$.

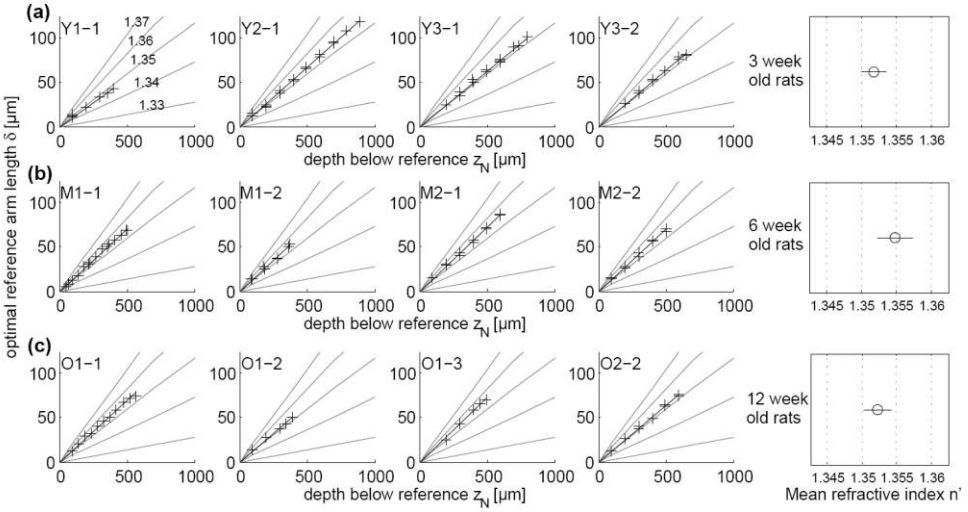

Fig. 3. For three 3 week old (a), two 6 week old (b) and two 12 week old (c) rats, the optimal reference arm length δ (see Fig. 2d) is plotted as a function of nominal imaging depth z_N. Each plot corresponds to one lateral position in one rat, e.g. plot "M1-2" corresponds to the second lateral position in the first 6 week old rat. For reference, the theoretical curves corresponding to fixed refractive index values from 1.33 to 1.37 are shown in all plots; the values are given in the upper left hand plot. These reference curves are fairly linear in the range of depths shown. From each plot, the mean slope δ/z_N was determined by least squares fitting and the refractive index n' was calculated. All values for different positions in animals of the same age were averaged to give the mean refractive index for animals of that age, shown in the right panel. One-way ANOVA showed no significant correlation between age and refractive index.

Since n' is a function of wavelength, an assumption about the dispersion (i.e. about the form of the function $n'(\lambda)$) needs to be made to be able to use Eq. (2). In contrast to the existing literature, our formalism is very flexible with respect to this assumption. While previous papers always assumed $n'(\lambda) = \text{const}$, we worked with the assumption $n'(\lambda) = n(\lambda)+\Delta n$. That is to say, we consider that the dispersion of the tissue will match that of water and that the refractive index is increased by a wavelength-independent quantity Δn. If the exact refractive index n'_0 of the tissue at a given wavelength λ_0 were known, the OCT defocus

#139111 - $15.00 USD Received 7 Dec 2010; revised 24 Jan 2011; accepted 2 Feb 2011; published 28 Feb 2011

measurement could alternatively be used to determine dispersion by setting $n'(\lambda) = n'_0 + (\lambda - \lambda_0)\frac{dn'}{d\lambda}$ and optimizing the integral in Eq. (2) for z_A and $\frac{dn'}{d\lambda}$.

Choice of metric

The optimal position where coherence volume and actual focus coincide can be determined by using one of several image-based metrics in ff-OCT. While Tearney et al. [11] used total signal intensity as a metric, Labiau et al. [12] applied the optimization of low spatial frequency content of normalized images as proposed by Debarre et al. [22] to ff-OCT. The latter method is useful in systems where aberrations degrade image quality without affecting signal strength, or when the sensitivity range of the metric needs to be tuned to a certain scale of aberrations. While the low and medium spatial frequency content of the images is sensitive to aberrations (Fig. 2e), we found that optimization of total OCT signal had superior signal to noise ratio. The refractive index values calculated with both metrics agreed within the measurement error (data not shown). Therefore, we used total intensity as the metric best suited for high-NA OCT defocus optimization.

This method of optimization was possible even at depths where no structure could be discerned in the images and where, in consequence, spatial frequency content-based metrics failed to find an optimum (data not shown). While imaging is not possible at such depths, the defocus value found can still be used to determine the refractive index.

Results

Rat brain refractive index as a function of rat age

To calculate the mean refractive index of the tissue, reference arm optimizations were performed at different nominal depths in 19 different lateral positions (fields of view) in the somatosensory cortex of 7 rats. Between two successive optimizations at different depths, an optimization at a fixed reference depth just below the tissue surface was performed. This allowed us to compensate for drifts (probably caused by temperature changes), which resulted in a change of optimal reference arm length.

In order to determine if the refractive index of the brain depends on the age of the animal, we used animals of different ages (3, 6 and 12 weeks old). In 3 weeks old rats, depths up to 900µm were accessible to refractive index measurements, while older animals allowed measurements only up to 600µm deep.

In order to calculate the refractive index of the rat brain, the optimal reference arm length δ for different nominal depths z_N below the reference depth was plotted (Fig. 3). The optimal reference arm length δ changed linearly with depth z_N in all animals and lateral positions (Fig. 3). One consequence of this good linearity is that the refractive index of the tissue is the same at different depths below the surface. An abrupt change of the refractive index would be indicated by a kink in the curves.

A depth-averaged value for the refractive index was then calculated for each field of view in each rat from the slope of the plots in Fig. 3. A one-way ANOVA was performed to compare the groups of rats of different ages (3 week old vs. 6 week old vs. 12 week old animals). It showed no significant correlation between the age of the animal and the refractive index of the cortex (Fig. 3). The uncertainty of the depth-averaged refractive index measurements was generally smaller than the lateral variations from one field of view to another, which were, in turn, comparable to differences between animals.

Finally, we computed the mean refractive index over all positions and all rats of all ages, which was found to be $n' = 1.3526 \pm 0.0029$ (std.dev.), ± 0.0007 (s.e.m.) for the wavelength range $\lambda = 1.1 \pm 0.1$ µm. It is important to note that the refractive index of water varies from $n = 1.3222$ to $n = 1.3252$ in this wavelength range [23].

#139111 - $15.00 USD Received 7 Dec 2010; revised 24 Jan 2011; accepted 2 Feb 2011; published 28 Feb 2011

Defocus-corrected ff-OCT imaging

As soon as defocus optimization at two different depths has been performed, the slope of the optimal reference arm length versus nominal imaging depth can be calculated. This approach was used to acquire ff-OCT z-stacks in the rat somatosensory cortex where the correct reference arm length for defocus compensation was applied automatically by the software for each z-slice which was taken (open-loop correction). This allowed us to perform *in vivo* imaging of rat somatosensory cortex to depths of several hundred microns. The OCT imaging frequency (33Hz) was fast enough to take the two images needed for optical sectioning before the respiration and heartbeat caused the cortex to move more than a small fraction of a wavelength. Even the movement of individual red blood cells in thin veins as well as the movement of leukocytes on the surface of larger vessels at the brain surface could be observed in real time (Fig. 4 as well as Media 1 & Media 2).

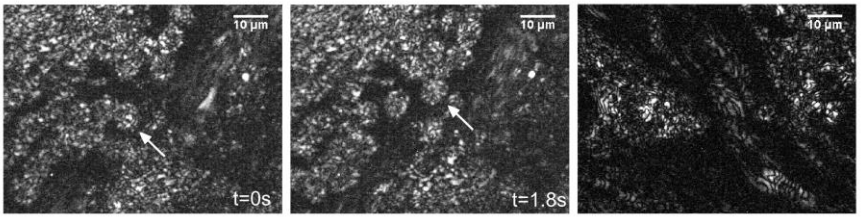

Fig. 4. Single-frame excerpts from ff-OCT video recordings of surface blood vessels in rat cortex. (Left/Center, Media 1) large vessel of a p46 rat; 6.6 Hz frame rate; produced from a 33 Hz video by averaging 5 ffOCT images each to increase signal to noise. In the upper left hand corner the tissue surrounding the vessel can be seen; passing from lower left to upper center individual leukocytes can be seen moving slowly along the vessel wall (one of them is marked with a white arrow). The right half of the field of view shows the interior of the vessel where objects move too rapidly to be resolved individually. In the lower center of the field of view, the vessel wall descends into the coherence volume so that leukocytes can be seen as if through a semi-transparent wall. (Right, Media 2) junction of two blood vessels joining in the cortex of a p21 rat. 4 seconds at 33Hz frame rate, taken without any averaging. In the upper vessel, an individual object can be seen which moves much slower than the surrounding blood, possibly due to interactions with the blood vessel wall.

The good linearity of optimal reference arm length with depth also implied that defocus-corrected imaging at arbitrary depths could be achieved using the measured slope, without re-optimizing defocus at every single depth. In Fig. 5, the loss of OCT signal with depth is shown. Without defocus correction (i.e. fixed reference arm length optimized at the sample surface), only 10% of the signal above background remains at around 120µm depth. With open-loop defocus correction based on the measured defocus slope, OCT signal falls off a lot more slowly; the 10% level is reached at about a 300µm depth, indicating a 2.5-fold increase in imaging depth. For comparison, depth intensity profiles are shown for fixed reference arm lengths which correspond to optimal defocus correction at depths of 200, 300 and 400µm, respectively.

#139111 - $15.00 USD Received 7 Dec 2010; revised 24 Jan 2011; accepted 2 Feb 2011; published 28 Feb 2011

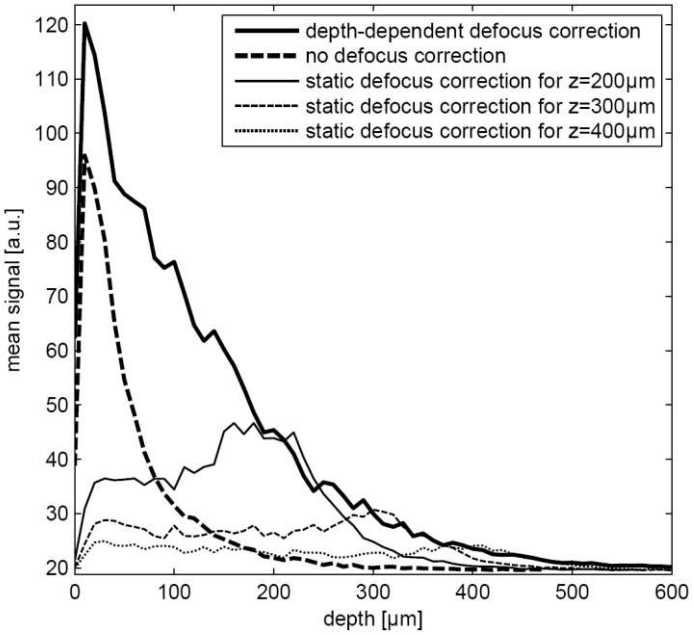

Fig. 5. The decrease of OCT signal with depth for different reference arm configurations shows the importance of defocus correction for penetration depth. Only with depth-dependent defocus correction is maximum signal at all depths achieved (thick solid line). Without defocus correction, the OCT signal decreases very rapidly (thick dashed curve). A fixed reference arm length optimized for imaging at depths of 200, 300 and 400µm, respectively, yields optimal signal at that depth but a low signal at all other depths (thin curves). The sample was the upper cortical layers of a young rat, imaged *in vivo* with ff-OCT at 33Hz. Each data point corresponds to the mean signal of four image frames taken at the same depth, corresponding to 120ms acquisition time. Axial scanning was performed with a 10µm step size.

Consequences for two-photon imaging

Due to the refractive index mismatch between the immersion water and the brain, paraxial rays have a shorter path to focus than marginal rays, leading to an aberrated (enlarged) point spread function. Since two-photon excitation efficiency depends quadratically on the local light intensity, the aberrations lead to signal loss, which can be quantified by describing the aberrations as a phase function (wavefront) in the objective pupil and then calculating the focal intensity distribution [24].

Using the measured value for the refractive index, we estimated the loss in resolution and signal in 2PLSM, for point-like objects as well as fluorescent planes and uniformly stained samples (Fig. 6). We assumed an objective with a NA of 1.0, fulfilling the sine condition, and a two-photon excitation wavelength of 1100nm. We assumed further that the objective is corrected for use with a coverslip so that the latter does not need to be taken into account in the calculation. Using the concept of high-NA defocus [25] under a refractive index mismatch [26], the wavefront corresponding to focusing at a given depth inside the sample was calculated. For the sample, a homogeneous refractive index with the experimentally determined value was used and a perfectly flat surface orthogonal to the optical axis was assumed, in the knowledge that experimental conditions with tilted and non-flat surfaces will further increase the aberrations. Using the non-paraxial Debye approximation [27], the two-photon excitation point spread function (PSF) was calculated for a given wavefront. Since typical two-photon lasers have a much smaller wavelength bandwidth (around 15nm FWHM) than the source used in our OCT experiments, dispersion has been neglected for this calculation.

#139111 - $15.00 USD Received 7 Dec 2010; revised 24 Jan 2011; accepted 2 Feb 2011; published 28 Feb 2011

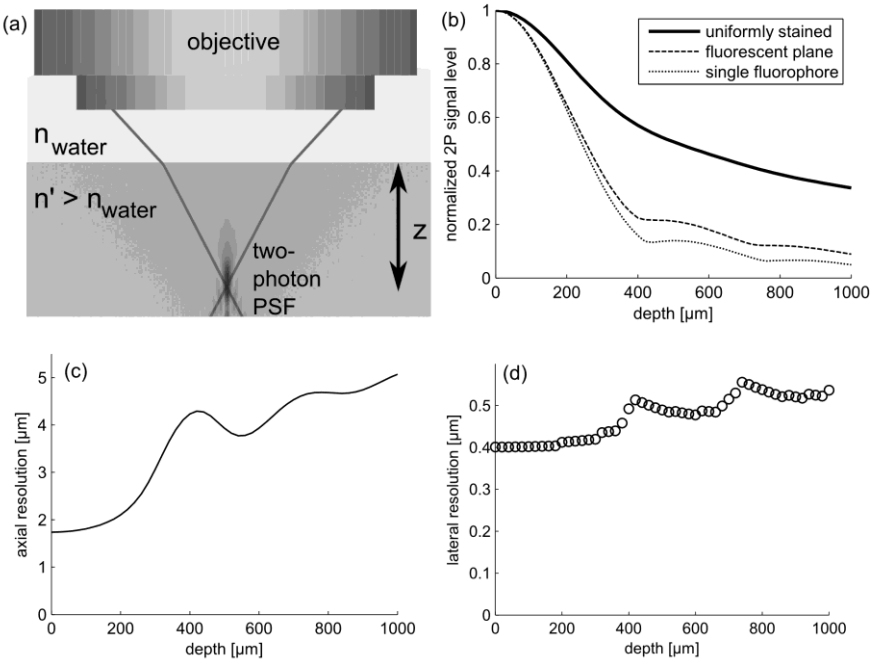

Fig. 6. Consequences of refractive index mismatch for 2PLSM. (a) Schematic drawing of the situation being simulated: a water immersion objective is used to focus a laser beam into a sample with refractive index n' which is larger than the refractive index n of the immersion medium. The aberrated two-photon excitation PSF for imaging at different depths z is calculated and analyzed. (b) Two-photon excitation loss caused by depth aberrations: for a single fluorophore (i.e. maximum of PSF), a fluorescent sheet (brightest xy plane of the PSF) and uniformly stained sample (3D integral of PSF). (c) Loss in axial resolution in 2PLSM (FWHM of response to fluorescent sheet, determined from a Gaussian fit to the simulated PSF). (d) Loss in lateral resolution in 2PLSM (FWHM of response to single fluorophore, determined from a Gaussian fit to the simulated PSF)

In calculating this PSF at different depths, the theoretical loss in lateral and axial resolution as well as the loss in two-photon excitation was determined – for a single fluorophore, for a fluorescent plane and for a uniformly stained sample.

As can be seen in Fig. 6, there is a steep drop in fluorescence excitation probability between the depths of 100 and 400µm, before reaching a plateau, where the decrease with depth is much smaller. At 400µm, an axially thin object such as a single fluorophore or a fluorescent membrane is excited with only 22% efficiency compared to the surface, due to a refractive index mismatch-induced spherical aberration, while fluorescence from an object larger than the aberrated focus is still excited with 57% efficiency.

To estimate the lateral resolution, a 1D-section through the calculated PSF was fitted with a Gaussian function, while the axial resolution was determined from fitting a Gaussian to the axial response to a fluorescent plane. The axial resolution is decreased by a factor of 2.5 in 400µm depth, while the lateral resolution decreases only by 20%. Due to the complicated form of the PSF beyond 400µm depth, it is meaningless to describe it with a single value for axial resolution.

Discussion

In this study we have measured the refractive index of rat cortex *in vivo* using defocus optimization in ff-OCT with high-NA objectives.

#139111 - $15.00 USD Received 7 Dec 2010; revised 24 Jan 2011; accepted 2 Feb 2011; published 28 Feb 2011

Importance of defocus correction for high-NA ff-OCT

Most scanning OCT systems are inherently limited to extremely low NA objectives, since their axial scan range is limited by the depth of field of the objective. In ff-OCT the sample is moved relative to the objective for z-scanning, so the scan range is only limited by the working distance of the objective and not by its NA. Higher NA can be used to increase the lateral resolution.

As shown here, a new problem arises with medium and high NA objective ff-OCT systems when the refractive index of the sample does not perfectly match the refractive index of the immersion medium. When imaging deeper layers, the additional optical path difference causes the coherence volume to move out of the depth of field of the objective; this defocus considerably decreases OCT signal and limits imaging depth when uncorrected. With a NA of 0.8, defocus correction increased the imaging depth 2.5-fold (Fig. 5), even though the refractive index of the cortex differed from water by only 2.2%.

In summary, signal level and penetration depth in ff-OCT imaging with high-NA objectives benefit greatly from defocus correction.

A model of defocus aberration in ff-OCT which takes into account high NA and dispersion

A high-precision refractive index measurement was achieved using large-NA objectives, which enhanced the sensitivity of the setup to small refractive index mismatches. In order to correctly analyze the data, both dispersion and NA must be taken into account, which our model does.

It was shown that the choice of assumptions about dispersion is important when the third and fourth digits after the decimal point of the refractive index are to be determined correctly. Our result for n' depends on the assumption that the dispersion in tissue equals the known dispersion of water. If we had neglected dispersion of both water and tissue, as has been done in previous work [11,12, 18–20], while still taking into account the NA (i.e. removed the integration over λ from Eq. (2) and worked with fixed n = 1.3237 corresponding to the center wavelength) our n' estimate would have been 0.0058 lower (underestimating the refractive index mismatch between tissue and water by 20%).

If, as well as neglecting dispersion, a paraxial approximation had been used [12], the refractive index would have been systematically overestimated by 0.0031 compared to our result, implying that the effect of dispersion and NA go in opposite directions in our case, with the effect of the NA being stronger. On the other hand, the marginal ray approximation by Tearney et al. [11] would result in an underestimation of n' by 0.0040. For an adaption of their formula to the case of immersion objectives, see the Appendix. To conclude, paraxial or marginal ray approximations are equally invalid at a NA of 0.8, justifying the use of a new model adapted to high-NA objectives and to broadband light sources.

Value and (non-dependence) of brain refractive index

Using our model, we have obtained a very accurate estimate of the phase refractive index of the rat brain cortex n' = 1.3526 ± 0.0029 (std.dev.), ± 0.0007 (s.e.m.) for the wavelength range λ = 1.1 ± 0.1 µm. This value allows for an evaluation of a lower bound for the scale of aberrations encountered in biological tissues. Independently of the absolute value, the lack of refractive index variation with age seems surprising. Apparently structural changes during development such as vascularisation and myelination of axonal fibers are not reflected in systematic changes of the refractive index.

Likewise, the lack of variation with depth inside the cortex is peculiar, given the lateral and inter-animal variability (±0.0029, see results). In particular, there seemed to be no difference in the refractive index of different cortical layers. It should be kept in mind that our spatial resolution for the refractive index measurement is determined laterally by the field of view of the microscope and the opening angle of the objective, while the axial sampling is determined by the distance between two measuring depths (usually 100µm). It could be that our measurements are not sufficiently spatially resolved to show existing changes with depth.

#139111 - $15.00 USD Received 7 Dec 2010; revised 24 Jan 2011; accepted 2 Feb 2011; published 28 Feb 2011

On the other hand, the lateral variations of the refractive index imply that a beam focused at some depth will encounter different refractive indices at different positions on the surface where it penetrates. This implies that other aberration modes such as astigmatism and coma will also play a role.

In two of the 3 week old rats, refractive index measurements were possible in depths considerably greater than in the older animals. It is unclear whether this is purely due to inter-individual and inter-positional variations or whether it is caused by increased scattering in the older animals [28], without at the same time affecting the refractive index.

Table 1.

Sample	Refractive index n'	Source	Measurement Wavelength [nm]
Human brain, gray matter	1.36 ±0.02 (std. dev.)	[7]	456/514/630/675/1064
Rabbit brain, gray matter	1.36 ±0.02 (std. dev.)	[7]	456/514/630/675/1064
Mouse brain slice (5µm, fixed)	1.368 ±0.007	[8]	633 nm
Cell body of mouse cortical neurons in culture (2 individual cells)	1.3751 ±0.0003 1.3847 ±0.0003	[9]	658 nm
Rat cortex, fresh 400µm slice	1.37	[10]	Unspecified; probably 830 nm or 1280 nm

In general, the refractive index measured here of 1.3526 ± 0.0007 (s.e.m.) was lower than most values found in the literature (Table 1). None of these values were measured *in vivo*, so it is possible that preparation issues such as loss of water or tissue degradation could have influenced these results. For example, slices of defined thickness were obtained using cryotomes (i.e. freezing the tissue) in some studies [7,8] and sometimes the tissue was slightly compressed to obtain a flat surface [7]. The cell bodies of neurons in culture is not necessarily a good comparison for the average refractive index of *in vivo* brain tissue. One other reason for the discrepancy could be that our measurements were performed in the near-infrared. Near infrared was chosen for improved ff-OCT and 2PLSM penetration depth [29–30]. At λ = 1.1µm, the refractive index of water (at 24°C) is already down to 1.3237 from the commonly cited value of 1.33 (which is valid around λ=700nm), and since tissue consists mainly of water, its index will more or less follow this trend. From the dispersion of water [23] and human skin dermis [31], we estimate the refractive index of the brain at λ=1.1µm to be about 0.007 to 0.01 lower than at λ=0.65 µm. Therefore, our measurement is on the lower bound of the published data, even considering dispersion. The variations of the refractive index from field to field, which were of the order of the inter-animal variations shows that a very accurate estimate of the refractive index requires its *in situ* measurement, which is now made possible by our *in vivo* approach.

Implication for aberrations in 2PLSM

The simulations presented here show that even though the refractive index of the rat brain is only slightly greater than that of water, the refractive index mismatch implies a considerable signal and resolution loss in 2PLSM due to optical aberrations, in particular at the large imaging depths possible today. Even in the most favorable case, where the refractive index is assumed to be homogeneous and the brain surface perfectly flat, our calculations show that diffraction-limited imaging is not possible beyond the first 200µm of tissue. 2PLSM in the living brain should therefore benefit from aberration correction using adaptive optics or even just a predefined, depth-dependent correction of the spherical aberration if no higher order aberrations exist.

Of course aberration correction should always be attempted starting from the most favorable circumstances. Currently available microscope objectives tend to be corrected for visible light. Therefore the assumption of a perfect objective is not valid at wavelengths in the near-infrared, and the intensity calculations performed here would only be valid after full correction of these system aberrations.

#139111 - $15.00 USD Received 7 Dec 2010; revised 24 Jan 2011; accepted 2 Feb 2011; published 28 Feb 2011

Apart from wavelength, the immersion medium is also important. For a water-based sample such as biological tissue, a water immersion lens should be used, whereas the use of glycerin embedded samples require the use of a glycerin immersion objective. To be able to make best use of high-NA oil immersion lenses, care must be taken to match perfectly the refractive index of the embedding medium of the fixed sample to the refractive index of the immersion oil. While several publications exist about correcting aberrations arising from violating this basic rule, only little work has been carried out to correct true sample-induced aberrations in 2PLSM caused by the small refractive index mismatch between water and tissue [3–4, 6]. In some of these latter cases, aberrations due to the shape of the sample surface were dominant. In 2PLSM of the brain, a coverslip is generally used to protect the tissue. If the bone around the craniotomy is appropriately thinned, the coverslip can be brought in direct contact with the brain tissue, ensuring a flat sample surface and removing surface-shape-associated aberrations.

Our results now show that even in this best-possible configuration with a water immersion objective, flat brain surface and assuming a homogeneous brain refractive index, correction of sample induced spherical aberration could drastically improve 2PLSM in the animal brain.

Appendix

The marginal ray calculation performed by Tearney et al. [11] assumes that the OCT signal is dominated by the light traveling at the highest angle. However, due to the coherent summation, it is rather the contribution from the area or areas of stationary phase that will dominate the integral in Eq. (2). Furthermore, their calculation assumes z_A to be fixed in relation to z_N based on the refraction of marginal rays; this need not necessarily be the case. In their experiments, the low NA (0.175) used implied a deviation from paraxial theory of only 0.5%, well below their experimental uncertainty. However, had their formula been applied at the NA of 0.8 used in this work, it would have caused a significant systematic error. Generalizing their formula (2) to the case with water immersion

$$n'_{marginal} \sin\left\{\arctan\left[\frac{n'_{marginal}\, z_N \tan\left(\arcsin\frac{NA}{n}\right)}{nz_N + \delta/2}\right]\right\} = NA \qquad (7)$$

we can calculate a “marginal ray refractive index”. For the mean defocus slope $\delta/zN=0.064886$, this would lead to $n'=1.3486$, which is an underestimation by 0.004 compared to the value found with our model, as mentioned in the main text.

Acknowledgements

This work was supported by ANR RIB grants MICADO n° ANR-07-RIB-010-02 and ANR-07-RIB-010-04. J.B. was funded by a PhD fellowship from the Fondation Pierre-Gilles de Gennes. We are deeply grateful to Boris Barbour and Sarah Mikula for their careful reading of the manuscript.

#139111 - $15.00 USD Received 7 Dec 2010; revised 24 Jan 2011; accepted 2 Feb 2011; published 28 Feb 2011